

A study of the central stellar populations of galaxies in SDSS-IV MaNGA: identification of a sub-sample with unusually young and massive stars

Guinevere Kauffmann^{1*}

¹*Max-Planck Institut für Astrophysik, 85741 Garching, Germany*

13 July 2021

ABSTRACT

This paper describes a search for galaxy centers with clear indications of unusual stellar populations with an initial mass function flatter than Salpeter at high stellar masses. Out of a sample of 668 face-on galaxies with stellar masses in the range $10^{10} - 10^{11} M_{\odot}$, I identify 15 galaxies with young to intermediate age central stellar populations with unusual stellar population gradients in the inner regions of the galaxy. In these galaxies, the 4000 Å break is either flat or rising towards the center of the galaxy, indicating that the central regions host evolved stars, but the H α equivalent width also rises steeply in the central regions. The ionization parameter [OIII]/[OII] is typically low in these galactic centers, indicating that ionizing sources are stellar rather than AGN. Wolf Rayet features characteristic of hot young stars are often found in the spectra and these also get progressively stronger at smaller galactocentric radii. These outliers are compared to a control sample of galaxies of similar mass with young inner stellar populations, but where the gradients in H α equivalent width and 4000 Å break follow each other more closely. The outliers exhibit central Wolf Rayet red bump excesses much more frequently, they have higher central stellar and ionized gas metallicities, and they are also more frequently detected at 20 cm radio wavelengths. I highlight one outlier where the ionized gas is clearly being strongly perturbed and blown out either by massive stars after they explode as supernovae, or by energy injection from matter falling onto a black hole.

Key words: galaxies: nuclei, galaxies: star formation, galaxies: stellar content, stars: Wolf Rayet, galaxies: bulges, galaxies: active

1 INTRODUCTION

Studies of the demographics of large samples of galaxies with active galactic nuclei in the local Universe have demonstrated that most present-day accretion occurs onto black holes with masses less than $10^8 M_{\odot}$ that reside in moderately massive galaxies ($10^{10} - 10^{11} M_{\odot}$) with high central stellar surface mass densities and young stellar populations (Kauffmann et al 2003). The volume-averaged ratio of star formation to black hole accretion in these systems is ~ 1000 (Heckman et al 2004), a value that is remarkably close to the the observed ratio of stellar mass to black hole mass in nearby galaxy bulges (Ferrarese & Merritt 2000, Gebhardt et al 2000). This implies that black hole growth and bulge growth through star formation are tightly coupled

Up to recently, combined studies of black hole and bulge growth in complete samples of galaxies have been confined

to data from optical single-fibre spectroscopic surveys at low redshifts (e.g. Kauffmann et al 2003; Kewley et al 2006), or joint analysis of X-ray imaging data and optical/near-infrared surveys of galaxies at higher redshifts (e.g. Hickox et al 2009). With the advent of integral field unit (IFU) spectroscopic surveys that measure spectra for hundreds of locations within each galaxy, it has become possible to study the spatial distribution and nature of the young stars and their surrounding ionized gas within growing bulges, thereby gaining detailed insight into the observed coupling between star formation and black hole formation in these systems.

It has long been recognized that high mass bulges with stellar masses greater than $\sim 3 \times 10^{10} M_{\odot}$ are similar to elliptical galaxies in having predominantly old and metal-rich stellar populations and in falling on much the same scaling relations between age/metallicity and bulge velocity dispersion as the ellipticals (Balcells & Peletier 1994; Terndrup et al 1994; De Jong 1996; Thomas et al 2005). Low mass bulges ($M_{*} \sim 10^9 - 10^{10} M_{\odot}$) exhibit much more scatter in both

* E-mail: gamk@mpa-garching.mpg.de

age and metallicity. Resolved spectroscopic studies of small bulge samples have shown that they exhibit a wide range of age and metallicity gradients, from negative to positive, indicating a diversity of formation histories and mechanisms (MacArthur et al 2009).

More than a half of galaxy bulges in late type galaxies with stellar masses in the range $10^8 - 10^{11} M_\odot$ contain nuclear star clusters (NSC) at their very centers. These are luminous and compact sources of excess light above the inward extrapolation of the host galaxy’s surface brightness profile that are found on scales of 50pc or less (see Neumayer et al 2020 for a recent review). The NSC at our own Galactic Center, first identified by Becklin & Neugebauer (1968) is the most well-studied of these systems. It appears to be intrinsically elliptical and flattened along the Galactic plane, with an axis ratio $b/a = 0.71$ (Schödel et al 2014). It is also rotating in the same direction as the Galactic disk (Genzel et al 1996). The central 0.5 pc region of the Milky Way NSC hosts 200 massive and young Wolf-Rayet and O- and B-type stars that are partitioned between two rotating disk-like structures (Genzel et al 2003; Levin & Beloborodov 2003). Because of the young ages (6-8 Myr) inferred for these stars, they are believed to have formed in situ within very dense, accreted gas. The initial mass function (IMF) of the stars inferred from their K-band luminosity function is inferred to be considerably flatter than Salpeter (Paumard et al 2006), though the exact form of the derived IMF appears to be quite sensitive to location within these structures (Lu et al 2018).

In external galaxies, all but the closest NSCs are barely resolved even with the Hubble Space Telescope. In general, the stellar populations of most nuclear star clusters are characterized by a dominant old stellar population plus a significant population of young stars. The NSCs also tend to be more metal rich than their surrounding host galaxy.

The formation of stellar mass black holes in NSCs and their possible evolution to intermediate masses through runaway collisions has been a topic of theoretical speculation for many years (see for example Rees 1978; Portegies Zwart & MacMillan 2002), but rather few observational constraints currently exist. One key unknown is the nature star formation in the extreme environments typical of galaxy centers. Our own Milky Way is believed to have had a relatively quiescent formation history. Questions such as “do most stars form with the same initial mass function in bulges as in galactic disks”, “what is the fraction of stars formed in bound systems rather than in isolation”, and “how does a very dense stellar and gaseous environment influence stellar evolution” remain largely unanswered for the galaxy population as a whole.

In this paper, I analyze the central stellar populations of a sample of 1000 galaxies with stellar masses in the range $10^{10} - 10^{11} M_\odot$ with face-on orientation and with IFU data from the Mapping Nearby Galaxies at APO (MaNGA) survey. Face-on galaxies are chosen so as to minimize the effects of dust attenuation and allow the stars in circumnuclear disk-like structures to be detected more easily (see Neumayer et al 2020). The goal of this paper is to identify bulges with central stellar populations indicative of “non-standard” phenomena, such as an excess of high mass stars compared to typical disk stellar populations.

Stellar population synthesis models are often used as a

way to constrain parameters such as the age, metallicity and IMF of a galaxy. Model-fitting is always subject to considerable systematic uncertainties that arise from a variety of different factors (see Conroy et al 2009 for a review). The approach that is taken here is empirical. Section 2 describes the observations and the sample selection. Section 3 examines scaling relations between three spectroscopic indicators of stellar age: the 4000 Å break strength, the Balmer absorption line index strength $H\delta_A$ and the $H\alpha$ line equivalent width corrected for dust attenuation. Strong correlations are found between these quantities in the outer galaxy. The majority of galaxies exhibit inner stellar population scalings that lie on the same relations as disks. In a minority of galactic bulge regions, there are strong deviations from the disk scalings.

In section 4, bulges with strongly deviating *central* stellar populations are identified by examining inner gradients for three stellar population indicators and how they correlate with each other. A bulge with a deviating central stellar population is defined as one where the correlations between the stellar indicator gradients differ strongly from those defined by the majority of the sample. Section 5 presents a detailed analysis of the stellar and ionized gas properties of the sample of bulges with unusual centers, comparing and contrasting the results with those found for control samples of bulges with “normal” central stellar indicator gradients. Section 6 presents some first insights from stellar population synthesis modelling and discusses possible ways to investigate linkages with black hole formation and accretion. Finally, the main results from the paper are summarized in Section 7.

2 THE PARENT GALAXY SAMPLE

The sample of galaxies is drawn from the 15th data release (DR15) of the Sloan Digital Sky Survey’s MaNGA project (Bundy et al 2015), which is part of the Sloan Digital Sky Survey IV programme (SDSS-IV; Blanton et al. 2017). The final MaNGA sample will consist of approximately 10,000 galaxies with redshifts $0.01 < z < 0.18$, spanning a wide range in galaxy morphologies and selected to be have an approximately flat distribution in terms of $\log(\text{stellar mass})$ (Yan et al. 2016; Wake et al. 2017). Observations are taken using the BOSS spectrograph (Smee et al. 2013) on the 2.5 m Sloan telescope at Apache Point Observatory (Gunn et al. 2006). The spectra have a wavelength range of 3600-10000 Å and a spectral resolution of $R \sim 2000$ (Drory et al. 2015). MaNGA’s individual IFUs consist of hexagonal fibre bundles containing 19-127 optical fibres (each with diameter 2 arcsec), with a threepoint dithering pattern employed during observations in order to fully sample the targeted field of view (Drory et al. 2015; Law et al. 2015). Observations are reduced through the MaNGA Data Reduction Pipeline (DRP; Law et al. 2016; Yan et al. 2016), which flux-calibrates and sky-subtracts spectra before drizzling observations onto spaxels of width 0.5×0.5 arcsec. Flux calibration is performed using standard stars observed with fibre bundles of 7 fibres apiece. The final reconstructed datacubes have a point-spread function (PSF) full-width at half-maximum (FWHM) of approximately 2.5 arcsec (Law et al. 2015).

DR15 includes data for 4,621 unique galaxies. The available data consists of the raw data from the first three years of the survey, the intermediate/final data reduction pipeline (DRP; Law et al 2016) products, and the first release of derived data products from the data analysis pipeline (DAP; Westfall et al. 2019; Belfiore et al. 2019). These derived data products include maps of emission line fluxes, gas and stellar kinematics, and stellar population properties. The DAP also includes model fits to the stellar continuum using the pPXF fitting routine (Cappellari & Emsellem 2004), which employs a stellar-template library constructed by hierarchically-clustering the MILES stellar library (Vazdekis et al 2016) into a set of 42 composite spectra, termed the MILES_{SHC}.

Once the stellar-continuum fit has been performed, the DAP analyzes the emission-lines by subtracting the best-fitting continuum model from the data. In this paper, the unbinned per-spaxel emission line and spectral line index measurements available from the MAPS files are used where possible. The MAPS files are the primary output file from the DAP and provide 2D “maps” (i.e., images) of DAP measured properties. Model LOGCUBE files, which provide the binned spectra and the best-fitting model spectrum for each spectrum that was successfully fit, are used to compute additional spectral parameters such as spectral “bumps” indicating the presence of Wolf-Rayet stars (see section 5 for more details).

Stellar masses and structural parameters such as position angles, ellipticities, and half-light radii for all galaxies in the MaNGA sample are available from the MaNGA *drpall* file; in all cases, the structural parameters are obtained from the SDSS elliptical Petrosian apertures. All galaxies with ellipticity parameter b/a greater than 0.7, half-light radii greater than 5 arcsecond and stellar masses in the range $10^{10} < \log M_* < 10^{11} M_\odot$ are selected. The stellar mass cut is adopted to confine this analysis to galaxies that are similar in mass to our Milky Way. As discussed in section 1, the cut on galaxies with near face-on inclination helps to minimize dust obscuration of young stellar populations near the centers of galaxies. The cuts yield a sample of 668 galaxies with flags that indicate good quality data.

Figure 1 presents the basic parameters of the galaxies in this sample. Histograms of stellar mass, redshift, global NUV-r colour (the NUV photometry is taken from imaging data by the GALEX satellite and is included as part of the NASA-Sloan Atlas ¹), r-band half light radius R_{50} and ellipticity parameter b/a are presented. As can be seen, the galaxies are distributed fairly evenly in stellar mass, colour and ellipticity within the selection boundaries. Almost all (93%) are located at redshifts less than 0.07 and the typical radius of the half-light region is 7-8 arcsec.

3 COMPARISON OF RADially AVERAGED INNER AND OUTER STELLAR POPULATIONS

The analysis begins by examining the correlations between 3 different indicators of the stellar age of a galaxy for the full sample of 668 galaxies. These are

- (i) The narrow definition of the 4000 Å break, defined as the ratio of the average flux densities F_ν in the bands 3850-3950 and 4000-4100 Å (Balogh et al. 1999). This index is denoted as $D_n(4000)$ throughout this paper.
- (ii) The $H\delta_A$ index (Worthey & Ottaviani 1997) with central index bandpass 4083.5 - 4122.25 Å.
- (iii) The $H\alpha$ emission line equivalent width, denoted EQW $H\alpha$.

These indicators all probe the age of the stellar population, but are sensitive to light from stars of different masses, and scaling relations between them should be sensitive probes of the stellar initial mass function (IMF).

When calculating the $H\alpha$ equivalent width, the $H\alpha$ line flux is corrected for dust attenuation using the measured Balmer decrement using the formula $A_V = 1.9655 R_V \log(H\alpha/H\beta/2.87)$, where $R_V = 3.1$ and the Calzetti (2001) attenuation curve have been adopted. The stellar continuum measurements are not corrected for dust attenuation. This is best done in the context of full-spectrum fitting using stellar population synthesis models and will be the subject of future work. This paper focuses on relative trends in directly measured quantities as a function of position within the galaxy.

For each galaxy, radially averaged values of each stellar indicator are evaluated in bins of R/R_{50} where R_{50} is the half-light radius. The bins range from 0.1 R/R_{50} to 1.5 R_{50} in steps of 0.1 R/R_{50} . Radially averaging serves to damp fluctuations caused by individual HII regions and results in tighter correlations than those produced by individual spaxel measurements.

Figure 2 compares correlations between the three indicators for stellar populations in the inner galaxy (defined as $R < 0.5 R_{50}$ and plotted as red points) with those in the outer galaxy (defined as $0.5 R_{50} < R < 1.5 R_{50}$ and plotted as black points). Results are shown separately for two mass ranges: $10 < \log M_* < 10.5 M_\odot$ (left panels) and $10.5 < \log M_* < 11 M_\odot$ (right panels) to investigate whether there are any systematic trends with the mass of the galaxy.

Radially averaged stellar populations occupy a very tight sequence in the plane of $H\delta_A$ versus $D_n(4000)$. Inner and outer stellar populations largely overlap each other with a hint of greater scatter for the inner galaxy stellar populations. The red points are more evenly spread along the $H\delta_A$ versus $D_n(4000)$ locus for lower mass galaxies than for higher mass galaxies, indicating a shift towards older ages in the bulges of higher mass galaxies. This is in accord with previous findings in the literature, as outlined in Section 1. In particular, the $H\alpha$ EQW distribution in the inner galaxy exhibits a 10% tail to values in excess of a few hundred; this tail is not seen in the outer galaxy. This will form the subject of more detailed investigation later in this paper.

The relation between $H\alpha$ equivalent width and $D_n(4000)$ shown in the bottom panel of Figure 2 exhibits considerably more scatter, particularly at large values of

¹ <http://nsatlas.org>

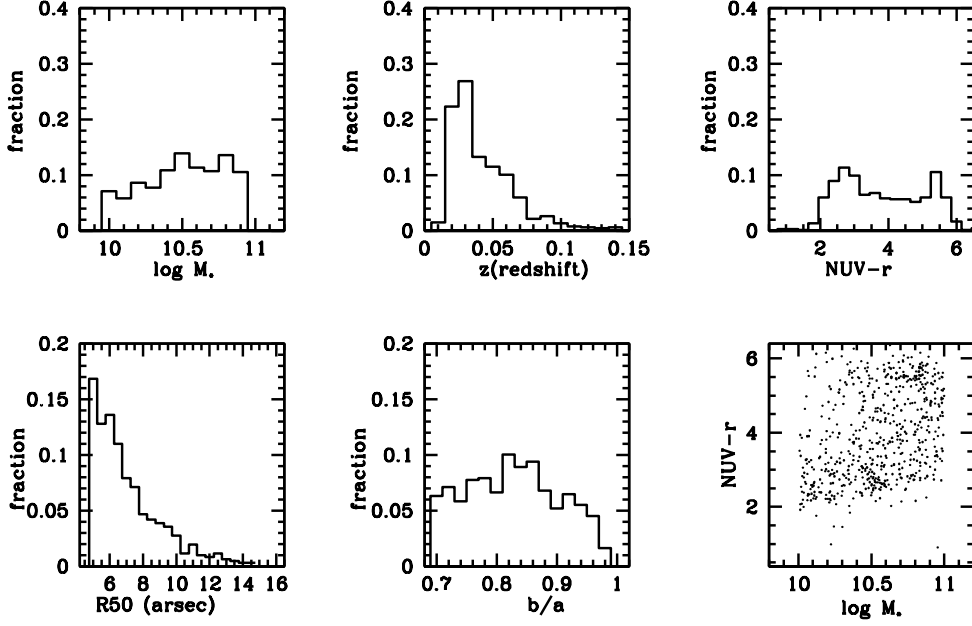


Figure 1. The global properties of the parent galaxy sample. Histograms of stellar mass, redshift, global NUV-r colour, r-band half light radius R_{50} and ellipticity parameter b/a are presented in the first 5 panels. The 6th panel shows a scatter plot of NUV-r colour versus stellar mass.

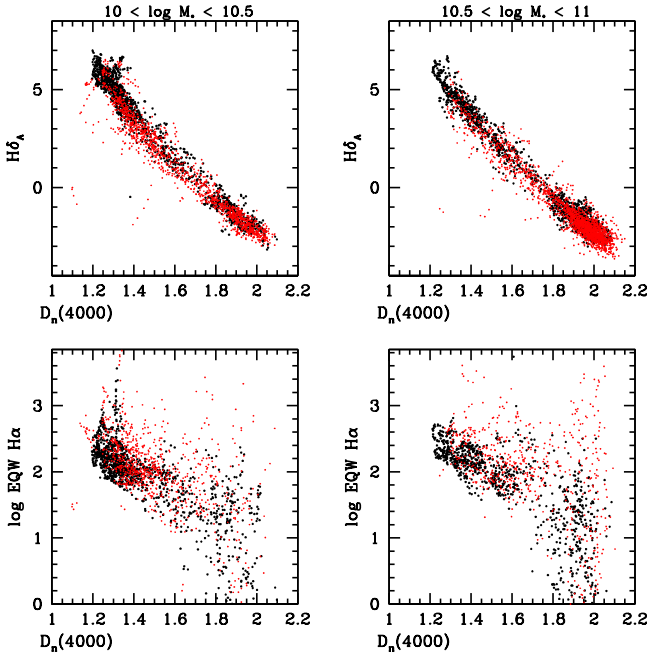


Figure 2. Correlations between the three indicators for stellar populations ($D_n(4000)$, $H\delta_A$ and EQW $H\alpha$) are shown for radially averaged measurements in the inner galaxy (defined as $R < 0.5 R_{50}$ and plotted as red points) and in the outer galaxy (defined as $0.5 R_{50} < R < 1.5 R_{50}$ and plotted as black points). Results are shown separately for two mass ranges: $10 < \log M_* < 10.5$ (left panels) and $10.5 < \log M_* < 11$ (right panels). All inner galaxy spaxels that have emission line ratios consistent with AGN ionization have been removed (see text).

$D_n(4000)$. One possible source of scatter in the central regions of galaxies not related to stars, is ionization from AGN. In order to minimize this effect, in the bottom two panels, we have made a cut in the $[\text{NII}]\lambda 6584/H\alpha$ versus $[\text{OIII}]\lambda 5007/H\beta$ BPT (Baldwin, Philips & Terlevich 1981) nebular emission line diagram, excluding all spaxels with emission line ratios that satisfy the AGN cut given in Kauffmann et al (2003):

$$\log([\text{OIII}]/H\beta) > 0.61/(\log([\text{NII}]/H\alpha) - 0.05) + 1.3. \quad (1)$$

This cut is only applied to spaxels from the inner regions of the galaxies and it removes 24% of the inner spaxels from galaxies in the low mass bin and 31% of spaxels from galaxies in the high mass bin. Even after exclusion of central spaxels that may be contaminated by AGN emission, we see a clear shift in the red points to higher values of $H\alpha$ equivalent width at fixed $D_n(4000)$. This is the first suggestion that the stellar populations in the central regions of galaxies are systematically different to those in the outer regions.

The results from Figure 2 are quantified in more detail in Figure 3, where solid red and black lines show the median relations between $H\delta_A$ and $D_n(4000)$ and $H\alpha$ equivalent width and $D_n(4000)$ for outer and inner stellar populations, respectively, while dashed and dotted lines show the 10th and 90th percentiles of the distribution of $H\delta_A$ and $H\alpha$ EQW at a fixed value of $D_n(4000)$. As in the previous figure, all inner galaxy spaxels that have emission line ratios consistent with AGN ionization have been removed. To make this figure, the radially averaged measurements are arranged in ascending order of $D_n(4000)$ and the median and percentiles are computed for bins containing 50 measurements. The up and down fluctuations in the lines should thus be regarded

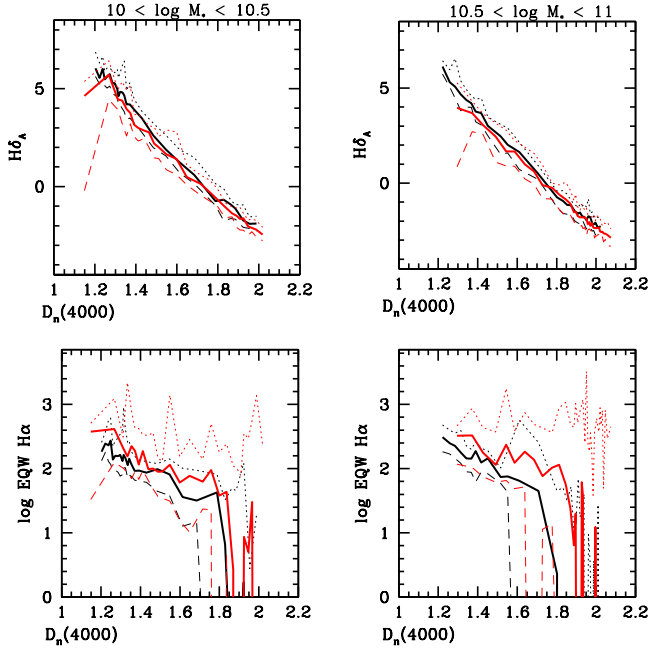


Figure 3. Red and black lines show the median relations between $H\delta_A$ and $D_n(4000)$ and $H\alpha$ equivalent width and $D_n(4000)$ for outer and inner stellar populations, respectively, while dashed and dotted lines show the 10th and 90th percentiles of the distribution of $H\delta_A$ and $H\alpha$ EQW at a fixed value of $D_n(4000)$. As in Figure 2, the results are shown in two stellar mass bins.

as a measure of the Poisson error in the evaluation of these quantities.

As can be seen, there is a small, but significant shift in the median $H\delta_A$ towards lower values at fixed $D_n(4000)$ for inner stellar populations compared to outer ones, and a larger shift in the median EQW $H\alpha$ towards high values for inner stellar populations. There is also a significant outlying population of bulges that have radially-averaged EQW $H\alpha$ values greater than a few hundred. Such large $H\alpha$ EQW values are largely absent in the outer stellar populations of galaxies. These outlier bulges will form the subject of a more detailed investigation in Section 4 of the paper.

4 INNER STELLAR POPULATION GRADIENTS

This section examines radial trends in the three age indicators, $H\delta_A$, $D_n(4000)$ and EQW $H\alpha$, and the degree to which these correlate with each other. Note that no cuts to remove AGN-contaminated spaxels are made in this section.

For each galaxy, the spaxel measurements are divided into 4 radial ranges: 0-0.3 R_{50} , 0.3-0.6 R_{50} , 0.6-0.9 R_{50} and 0.9-1.2 R_{50} . The slope is determined by linear least squares regression. The index difference is denoted Δ and is defined as the difference in the best fit index value at the two end-points of the radial range: for example, $\Delta D_n(4000)$ (0.3-0.6 R_{50}) is the difference in the linear fit to 4000 Å break strength versus R/R_{50} evaluated at 0.3 R_{50} and at 0.6 R_{50} .

Figure 4 shows three index differences for 4 differ-

ent radial ranges as a function of the NUV-r colour of each galaxy. Results for galaxies in the stellar mass range $10 < \log M_* < 10.5 M_\odot$ are shown in the first part of Figure 4 and for galaxies in the mass range $10.5 < \log M_* < 11 M_\odot$ in the second part. As can be seen, gradients in the stellar age indicators are strongest in the innermost regions of blue galaxies with $NUV-r < 4.5$ and become progressively weaker at larger radial distances. The majority of blue galaxies have negative $D_n(4000)$ gradients and positive $H\delta_A$ gradients in their inner regions, indicating that stellar populations become progressively older (higher $D_n(4000)$ and lower $H\delta_A$) towards the centres of most galaxies. The typical $H\alpha$ EQW profile is relatively flat in blue galaxies with $NUV-r < 4.5$, but increases towards the central regions in red galaxies with $NUV-r > 4.5$, which likely indicates a greater contribution from AGN rather than from stellar ionization sources in red systems.

Results for the low mass and high mass subsamples shown in Figures 4 are qualitatively similar. One difference is that at intermediate NUV-r colours of $\sim 3.5 - 4.5$, there are around a dozen galaxies in the lower mass sample where the $D_n(4000)$ profile is flat in the 0-0.3 R_{50} radial bin, but where $H\delta_A$ is rising towards the central regions of the galaxy. These are likely “post-starburst” bulges, where there has been a significant central burst of star formation a few hundred million years to 1 Gyr in the past. Hot O and B-type stars have already evolved off the main sequence in these bulges, but there is still a significant contribution from A to F-type stars that results in strong Balmer-line absorption in their centres. In the high stellar mass bin, the $D_n(4000)$ and $H\delta_A$ profiles in the central radial bin appear to track each other in almost all galaxies irrespective of colour.

Figure 5 examines correlations between the index differences for the central 0-0.3 R_{50} radial bin. The reader is reminded that the focus of this paper is the question of whether there is a population of bulges where there is evidence for an excess population of young massive stars similar to that claimed for the central region of our Milky Way. The presence of young, massive stars is probed directly by $H\alpha$ line emission, so it is intriguing that a population of apparent outliers is found in the plane of $\Delta(\log \text{EQW } H\alpha)$ versus $\Delta(D_n(4000))$ consisting of objects with very negative $\Delta(\log \text{EQW } H\alpha)$ indicative of steeply peaked central $H\alpha$ emission, but small $\Delta(D_n(4000))$ indicating weak variations in the age of the older stellar populations in the central regions of these galaxies. A cut

$$\Delta(\log \text{EQW } H\alpha) < (1.0/(-0.222))\Delta(D_n(4000)) + 0.026 - 0.6(2)$$

indicated by a red line in the middle panels of Figure 5 is used to pull out these systems, which are plotted as magenta points. As can be seen, these systems do not stand out in the plane of $\Delta H\delta_A$ versus $\Delta D_n(4000)$, indicating that the underlying older stellar population follows close-to-normal relations in these galaxies.

In the left panel of Figure 6, individual spaxel measurements are plotted in the plane of $\log \text{EQW}(H\alpha)$ versus $D_n(4000)$ for 10 out of the 13 outlying galaxies shown as magenta points in Figure 5.² The spaxel measurements are

² We do not show all objects to avoid overcrowding the plot. We have selected the 10 objects with the most inner spaxel measure-

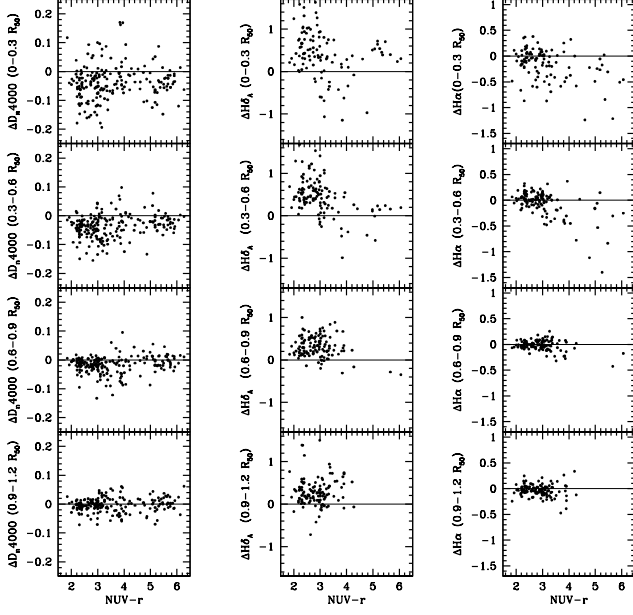


Figure 4. The index differences $\Delta D_n(4000)$, $\Delta H\delta_A$ and $\Delta \log \text{EQW}(\text{H}\alpha)$ are plotted as a function of the NUV-r colour of the galaxy. Results are shown in three rows for 3 different radial ranges for galaxies with stellar masses in the range $10 < \log M_* < 10.5 M_\odot$.

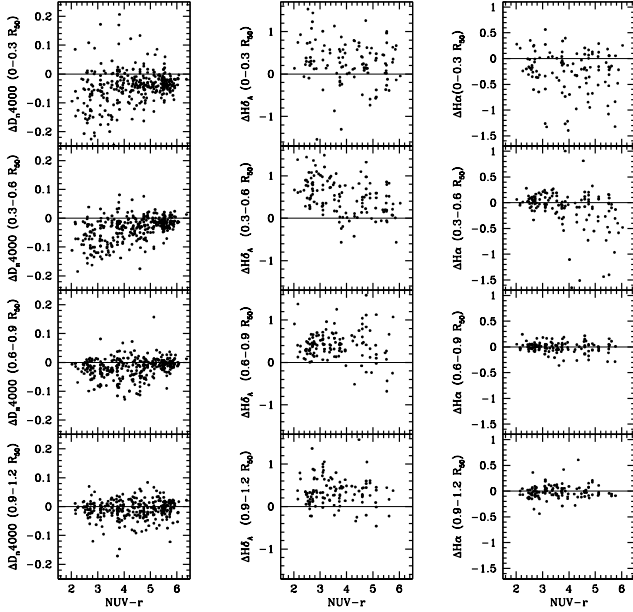


Figure 4 – continued Same as the previous sub-figure, except for galaxies with stellar masses in the range $10.5 < \log M_* < 11 M_\odot$.

restricted to those within $1.2 R/R_{50}$ and where the signal to noise in both the $\text{H}\alpha$ and $\text{H}\beta$ line measurements are greater than 3, allowing for reasonably accurate estimation of the Balmer decrement. The plot includes spaxels for all outliers in the stellar mass range $10 < \log M_* < 10.5$. Results for outliers in the higher stellar mass bin are similar). Central ($R < 0.5 R_{50}$) spaxel measurements from a subset of the outliers are plotted as coloured points. All points of the same colour come from the same galaxy.

The central measurements form tight sequences in the $\log \text{EQW}(\text{H}\alpha)$ versus $D_n(4000)$ plane, indicating that there is a strong and systematic offset in the physical properties of the entire central region of the galaxy, not just in a handful of isolated regions. It can also be seen that the spaxel measurements separate into two main groupings at a $D_n(4000)$ value of ~ 1.6 , indicated by a dashed line on the plot. In the right panel of Figure 6, the central spaxels are plotted in the $[\text{OIII}]/\text{H}\beta$ versus $[\text{NII}]/\text{H}\alpha$ BPT diagram. Central spaxels where $D_n(4000) < 1.6$ are coloured in blue and those with $D_n(4000) > 1.6$ are coloured in red. As can be seen, galaxies with central spaxel values of $D_n(4000) < 1.6$ have low central ionization parameters, indicating that the source of the excess $\text{H}\alpha$ emission must be young stars rather than a central AGN. Although some of the spaxels lie just above the Kauffmann et al (2003) demarcation curve separating AGN from star-forming galaxies, the fact that the $\text{H}\alpha$ equivalent widths are greater than 100 rule out ionization by evolved, post-AGB stars (Belfiore et al 2016). The small cloud of blue points in the high ionization region of the BPT diagram all come from a single galaxy, which is discussed in detail in section 6.2 and is postulated to be a galaxy in transition between star-forming and quiescence, because the $\text{H}\alpha$ line profiles exhibit clear outflow signatures. The distribution of the red points in the BPT diagram shows that a much larger fraction of the galaxies with $D_n(4000) > 1.6$ have high central ionization parameters indicative of AGN heating processes. Because the interpretation of these objects in terms of their stellar properties is less straightforward, these galaxies will not be considered further in this paper and all further analysis is restricted to the sub-sample of outliers with central spaxel values of $D_n(4000) < 1.6$.

5 PROPERTIES OF THE LARGE $\text{H}\alpha$ EQW OUTLIER GALAXIES

This section characterizes the radial profiles of a sample of 15 galaxies with outlying central stellar populations in the plane of $\log \text{EQW}(\text{H}\alpha)$ versus $D_n(4000)$, where the average value of $D_n(4000)$ for spaxels contained within $0.3 R_{50}$ is less than 1.65. The galaxies are selected from the full stellar mass range spanned by our parent sample. A “control sample” of 15 galaxies with similar central $D_n(4000)$ values, stellar masses and redshifts, which are not classified as outliers in the $\text{EQW}(\text{H}\alpha)/D_n(4000)$ plane is extracted in order to characterize which aspects of the radial trends are unique to the outlier population.

ments that exhibit the largest dynamic range in $\text{EQW}(\text{H}\alpha)$. These tend to be the most nearby objects.

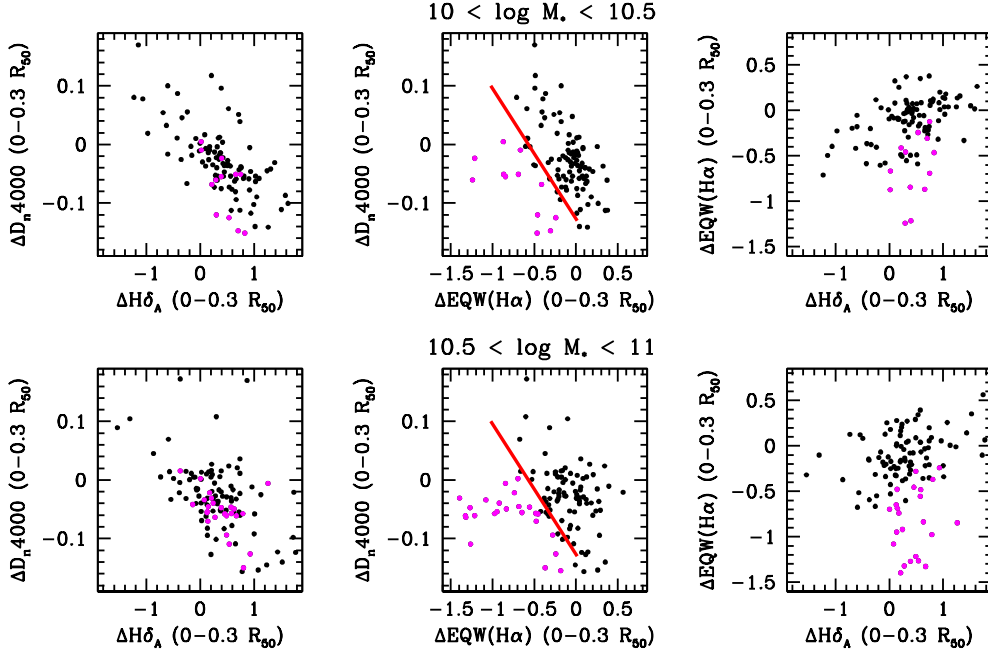


Figure 5. Correlations between the index differences for the central $0-0.3 R_{50}$ radial bin. Results for galaxies in the stellar mass range $10 < \log M_* < 10.5 M_\odot$ are shown in the upper panels and for $10.5 < \log M_* < 10.5 M_\odot$ in the lower panels. The cut indicated by the red line in the middle panels is used to define the outlier sample with unusually steeply centrally rising EQW $H\alpha$ profiles.

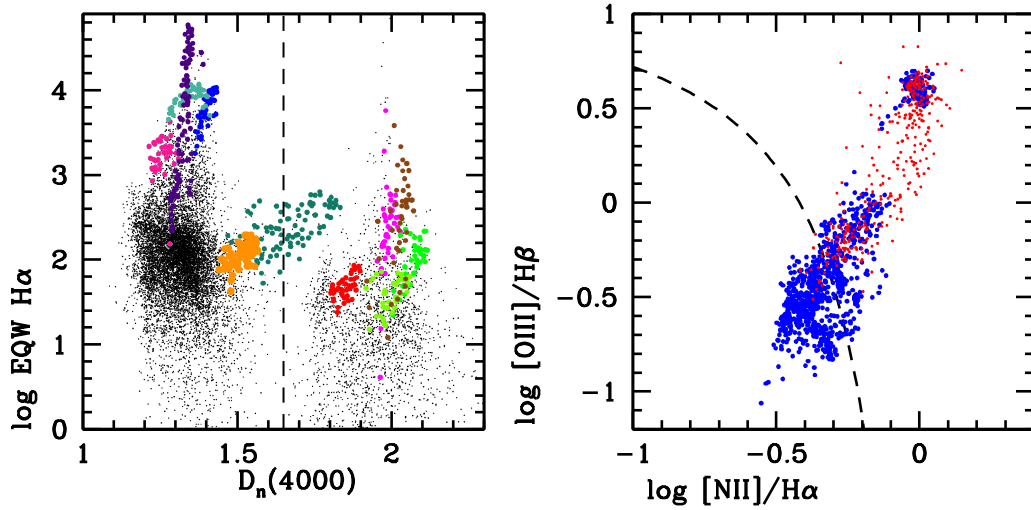


Figure 6. Left: Individual spaxel measurements for galaxies in the stellar mass range $10 < \log M_* < 10.5 M_\odot$ are plotted in the plane of $\log EQW(H\alpha)$ versus $D_n(4000)$ for the outlying galaxies shown as magenta points in Figure 5. The spaxel measurements are restricted to those within $1.2 R/R_{50}$ and these are plotted as black points. Central ($R < 0.5 R_{50}$) spaxel measurements from a subset of the outliers are plotted as coloured points. All points of the same colour come from the same galaxy. Right: Location of the central ($R < 0.5 R_{50}$) spaxels in the $[OIII]/H\beta$ versus $[NII]/H\alpha$ BPT diagram. Central spaxels with $D_n(4000) < 1.6$ are plotted in blue and those with $D_n(4000) > 1.6$ are plotted in red.

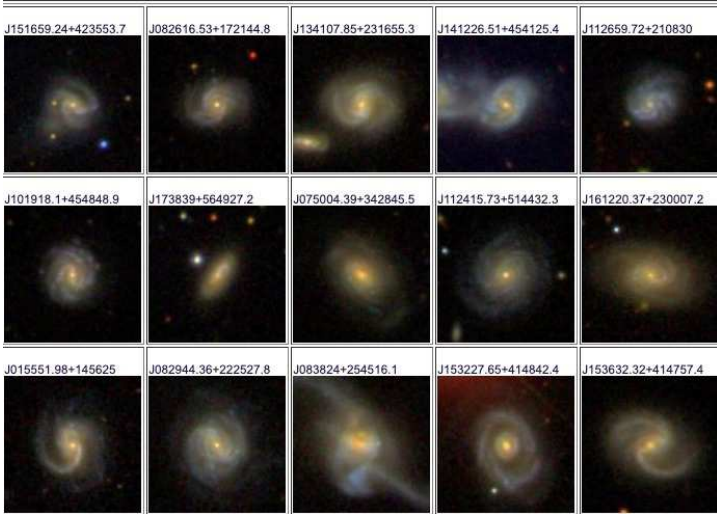


Figure 7. SDSS *g, r, i* colour images of the outlier sample.

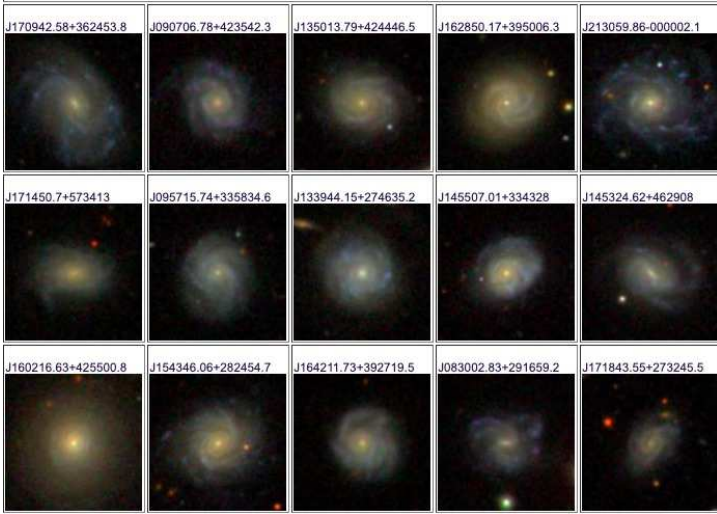


Figure 7 – continued SDSS *g, r, i* colour images of the control sample.

SDSS *g, r, i* colour images of the outlier and control samples are shown in Figure 7. There are three clearly interacting galaxies among the outliers (top row, columns 3 and 4, and bottom row, column 3). In addition, there are a number of clearly lopsided systems and galaxies with strong-armed spiral features suggestive of ongoing tidal interactions. In contrast, the control sample does not contain any interacting systems and consists of galaxies with more flocculent spiral structure.

In order to search for signatures of the presence of young, massive stars, the methodology described in Brinchmann et al (2008) has been implemented to identify Wolf Rayet features in the spectra. The main Wolf-Rayet features seen in the optical spectra of galaxies are two broad emission features: the blue bump around 4600–4680 Å (rest-frame) and the red bump around 5650–5800 Å (rest-frame). Brinchmann et al define an excess flux above the best-fit continuum in regions around the main Wolf-Rayet features. The continuum fits provided by the DAP (see section 2) are used to define the excess in the blue/red WR features as

$e_{\text{blue/red}} = F_{\text{central, blue/red}} - F_{\text{continuum, blue/red}}$ where F_{central} is the summed flux around the central wavelength of each feature and $F_{\text{continuum}}$ is the summed flux from the continuum fit in two wavelength intervals around each feature. The central wavelength positions are given in Table 1 of Brinchmann et al. The central and continuum passbands both span a width of 100 Å in total.

The blue Wolf Rayet feature includes the broad HeII emission line at 4686 Å that can sometimes be seen as a separate narrow feature. This is of potential interest because binary evolution models (e.g. Eldridge & Stanway 2009) predict elevated HeII emission for a longer period of time than models without binary stars. Because the line is often asymmetric, no attempt to fit a Gaussian is made, but the flux on either side of 4686 Å is summed until the first measured flux point dips below the continuum fit.

Finally, evidence of complex ionized gas kinematics is analyzed by searching for the presence of multiple components in the Hα emission line profile. The DAP includes the Gaussian model fit for each emission line after subtraction of the best-fit continuum. The presence of outflowing gas is manifested as an excess with respect to a single Gaussian fit on the blue side of the line (see for example Forster-Schreiber et al 2018). The reason we only look on the blue side is because a non-Gaussian component on the red side of the line will be blended with [NII]λ6584. The excess is parametrized as $F_{\text{non-Gaussian}}$, the fraction of the total Hα line flux shortwards of 6563 Å that is in excess of the single Gaussian fit provided by the DAP.

Figure 8 shows montages of radial profiles for two examples of outlier galaxies, while Figure 9 shows the same for two example control galaxies. A minimum S/N cut of 3 is imposed on all emission line fluxes and stellar continuum indices that are shown. Results are plotted out to a distance of 1.2 R_{50} where the majority of spaxel measurements meet this criteria. Magenta, red, green and blue points in each panel indicate spaxels in the radial ranges 0–0.3 R_{50} , 0.3–0.6 R_{50} , 0.6–0.9 R_{50} , and 0.9–1.2 R_{50} , respectively.

Significant variations in profiles are found between different galaxies from the two samples. The second galaxy shown in Figure 8 has a flat Hα equivalent width profile all the way from the central region to 1.2 R_{50} , but $D_n(4000)$ drops steeply out to 0.5 R_{50} and then flattens. No blue Wolf Rayet excess is detected at any radius, but the red Wolf Rayet excess increases towards the central regions of the galaxy at $R < 0.5 R_{50}$. The galaxy has a rather flat ionization parameter ([OIII]/[OII]) profile and a Balmer decrement profile that rises gently in the inner region to a value of ~ 6 . The gas-phase metallicity, as measured by the parameter $R23 = ([\text{OII}]\lambda 3727 + [\text{OIII}]\lambda 5007)/\text{H}\beta$, and the stellar absorption line index Mgb, which is most sensitive to the alpha element Magnesium, both have flat gradients across the galaxy. In contrast, the first galaxy shown in Figure 8 has a Hα equivalent width profile that rises steeply towards the central regions of the galaxy, and a $D_n(4000)$ profile that is flat. A small central blue Wolf Rayet excess is detected, but no central red excess is found. The galaxy also has a very steeply centrally rising Balmer decrement, but a gas-phase metallicity gradient that decreases towards the central regions.

The two control sample galaxies shown in Figure 9 show a similar degree of variability, especially in stellar and gas-

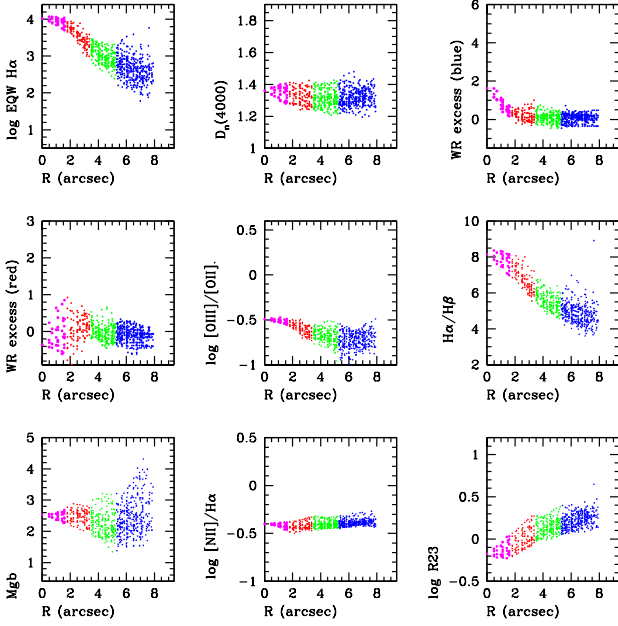


Figure 8. Radial profiles for a variety of stellar and ionized gas diagnostics. Magenta, red, green and blue points show spaxel located within $0-0.3 R_{50}$, $0.3-0.6 R_{50}$, $0.6-0.9 R_{50}$, and $0.9-1.2 R_{50}$, respectively. These results are for the outlier galaxy in the second row, third column in the first montage in Figure 7.

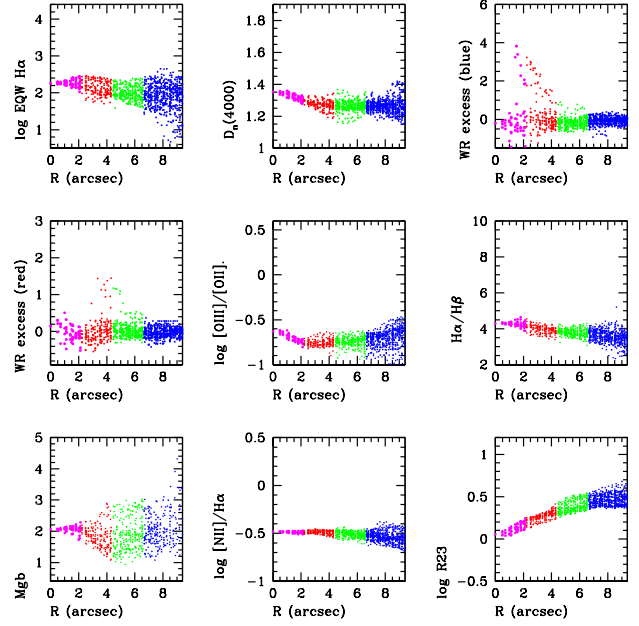


Figure 9. Radial profiles for a variety of stellar and ionized gas diagnostics. Magenta, red, green and blue points show spaxel located within $0-0.3 R_{50}$, $0.3-0.6 R_{50}$, $0.6-0.9 R_{50}$, and $0.9-1.2 R_{50}$, respectively. These results are for the control galaxy in the top row, first column in the second montage in Figure 7.

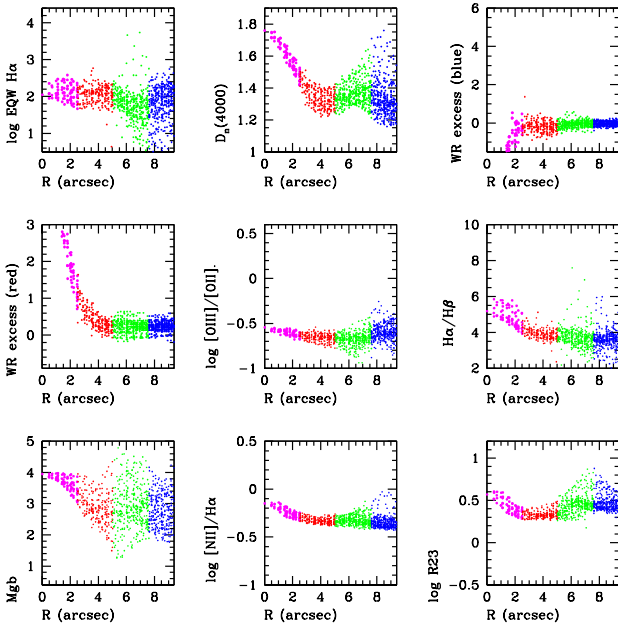


Figure 8 – continued Same as the previous figure, except for the outlier galaxy shown in third row, fourth column in the first montage in Figure 7.

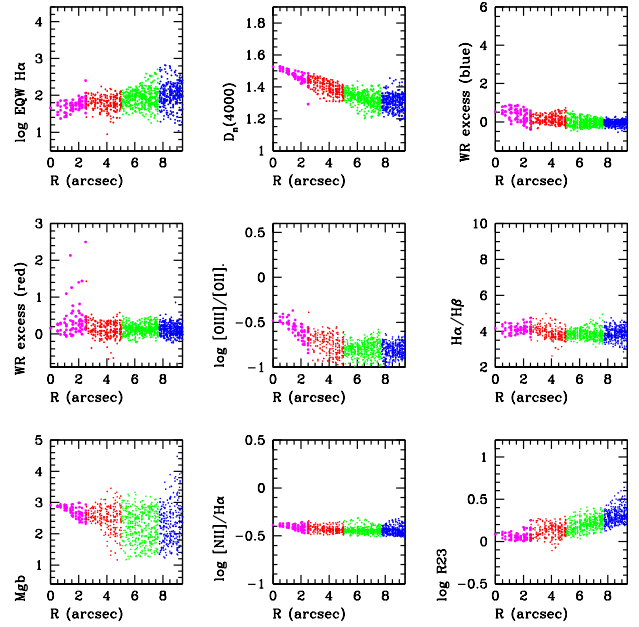


Figure 9 – continued Same as the previous figure, except for the control galaxy shown in top row, third column in the second montage in Figure 7.

phase metallicity indicators. It is thus clearly important to systematize the comparison between the outlier galaxies and the control sample. Values in the central spaxels are recorded for quantities that are independent of the selection procedure (e.g. [OIII]/[OII]). Emission line and stellar absorption index profiles are classified according to whether the quantity under study rises or falls towards the central regions of the galaxy, or is flat. Because the Wolf Rayet excess parameters, the HeII line equivalent widths and the non-Gaussian H α line shape measures are based on weak features in the spectrum and are more sensitive to systematic problems such as offsets in the stellar continuum fits, the galaxy is classified according to whether it exhibits a clear excess in these measurements in the central region compared to the outskirts.

The main results are summarized as follows:

(i) **log H α equivalent width:**

Outliers: 13 rising, 2 flat

Controls: 2 rising, 6 flat, 7 falling

(ii) **D $_n$ (4000):**

Outliers: 12 rising, 2 flat, 1 falling

Controls: 9 rising, 6 flat

(iii) **log H α /H β :**

Outliers: 13 rising, 2 flat

Controls: 3 rising, 12 flat

(iv) **log [OIII]/[OII]:**

Outliers: 13 rising, 2 flat, median central value: -0.5

Controls: 7 rising, 7 flat, 1 falling, median central value: -0.6

(v) **Blue WR central excess:**

Outliers: 6 yes, 9 no

Controls: 3 yes, 12 no

(vi) **Red WR central excess:**

Outliers: 12 yes, 3 no

Controls: 4 yes, 11 no

(vii) **HeII central excess:**

Outliers: 3 yes, 12 no

Controls: 3 yes, 12 no

(viii) **non-Gaussian H α central excess:**

Outliers: 1 yes, 14 no

Controls: 0 yes

(ix) **Mgb Lick index:**

Outliers: 11 rising, 4 flat, median central value: 2.5

Controls: 6 rising, 5 flat, 4 falling, median central value: 2.0

(x) **R23 index:**

Outliers: 4 rising, 4 flat, 7 falling median central value: 0.25

Controls: 2 rising, 3 flat, 10 falling, median central value: 0.0

(xi) **log [NII]/H α :**

Outliers: 7 rising, 8 flat, median central value: -0.3

Controls: 3 rising, 12 flat, median central value: -0.5

(xii) **VLA FIRST radio detection:**

Outliers: 8 yes, 7 no

Controls: no detections

Findings (i), (ii) and (iii) are direct consequences of the selection procedure used to define the outlier sample. Taken together, these three results show that the outlier sample consists of galaxies with more centrally peaked H α emission and that these regions are strongly obscured by dust. Finding (iv), showing that the central ionization parameter is only marginally higher for the outliers compared to the controls, indicates that young stars are the most probable central ionizing sources in both samples. The fact that

the ionization parameter is more often centrally rising in the outliers, indicates a possible systematic change in the nature of the ionizing stars with radius in these galaxies.

The suggestion that the outliers host a systematically different population of young stars in their centres is further strengthened by findings (v) and (vi), which show that a central Wolf Rayet excess is more frequently found in the outliers. The fact that the red Wolf Rayet excess is more common than the blue Wolf Rayet excess is particularly intriguing, because it indicates that these central starbursts are very different to those in UV-selected Wolf Rayet galaxies; this will be discussed in more detail in the next section.

Findings (vii) and (viii) are concerned with very weak spectral features that are at the limit of detectability. The results indicate that the [HeII] λ 4686 line is not the dominant contributor to the blue Wolf Rayet excess in all the outliers. The lack of clear non-Gaussian signatures in the H α line shows that if there are accreting black holes hidden in the central regions of these galaxies, they are not usually driving noticeable outflows of ionized gas. The case of the outlier with a clear H α outflow signatures will be discussed in detail in the next section.

Findings (ix), (x) and (xi) show that the outliers more often have centrally rising gas-phase and stellar metallicities compared to the control galaxies, and that their central metallicities are also systematically higher. This accords with finding (iii) that the outliers have higher central dust content (dust attenuation and metallicity are usually quite strongly correlated in star-forming systems).

Finally, finding (xii) that 53% of the outliers have detectable 20 cm radio emission compared to 0% of the control galaxies deserves some comment. The radio fluxes of the detected galaxies range from 1 mJy (the detection limit of FIRST) to 90 mJy, with a median value of 2.2 mJy. Even the brightest sources are unresolved at the 5 arcsec resolution of the FIRST observations. This again supports the conclusion that the central sources in the outliers are likely stellar rather than AGN.

6 DISCUSSION

In this section, a number of broader issues and unanswered questions arising from this work are discussed.

6.1 Inferences from stellar population synthesis models

The analysis so far has been empirical in approach. Starting from a sample of ~ 700 galaxies, the locus occupied by disk stellar populations in the plane of H δ_A versus D $_n$ (4000) and H α equivalent width versus D $_n$ (4000) is defined. Galaxies with central stellar populations that deviate strongly are identified. Once the outlier sample has been selected, radial trends for a variety of stellar and ionized gas diagnostics are studied in order to show that signatures from very young massive stars become progressively stronger towards the very centers of these galaxies. Because H α is sensitive to the presence of only the most massive stars, these results suggest that stars may be forming in these systems with an initial mass function (IMF) that is significantly different to that in galactic disks.

Stellar population synthesis modelling is, in principle, an important way to test whether these inferences accord with theoretical expectations and to quantitatively constrain parameter changes in the IMF. In practice, models of massive star evolution have many uncertain aspects, such as the effect of rotation, treatment of binary stars and their evolution, mass loss, and so on (see for sample Smith (2014) for a review). I will not delve very deeply into these matters in this paper, but will show some illustrative comparisons using the publically available Starburst 99 code (Leitherer et al 1999; 2014) to predict the H α equivalent width of galaxies and models from Bruzual & Charlot (2003) to predict the stellar continuum indices $D_n(4000)$ and $H\delta_A$.

In Starburst 99, it is necessary to combine a variety of inputs from very heterogeneous sources. The 4000 Å break and $H\delta_A$ predictions are generated using the high resolution stellar library in Martins et al (2005) consisting of synthetic stellar spectra. The predicted relation between $D_n(4000)$ and $H\delta_A$ differs significantly from other models that use empirical libraries (e.g. Bruzual & Charlot 2003) and is also significantly offset from the data shown in Figures 1 and 2. Unfortunately, the models that generate better fits to the stellar continuum features do not include detailed predictions for nebular features in the spectra. In this work, predictions for H α luminosity evolution for a simple stellar population (SSP) as a function of time are taken from Starburst99 and are matched to the evolution of the stellar continuum fluxes from the Bruzual & Charlot (2003) models at the same output times. The top two panels of Figure 10 show loci occupied by galaxies in the $H\delta_A$ versus $D_n(4000)$ (left) and EQW H α versus $D_n(4000)$ planes (right) occupied by galaxies that have had continuous star formation histories. All model galaxies begin forming stars 9 Gyr in the past and their star formation rate is parametrized as $SFR(t) = Ce^{\gamma t}$, where γ varies over the range -2.0 to 0.0, i.e. from steeply declining to constant star formation rate as a function of time. Black, green and blue curves show results for solar, 0.5 solar and 0.25 solar metallicity models. A standard Kroupa (2001) initial mass function has been adopted. This IMF has the standard Salpeter slope $\alpha = 2.3$ above half a solar mass, but introduced $\alpha = 1.3$ between 0.08-0.5 M_\odot and $\alpha = 0.3$ below 0.08 M_\odot . This IMF is widely adopted when fitting normal galaxy stellar populations because it provides simultaneous good fits to the observed mass-to-light ratios and colours of nearby spiral galaxies (e.g. McGaugh & Schombert 2014).

The bottom two panels show how recent bursts superposed upon the grid of models with continuous star formation histories and solar metallicity influence the predicted location in the two planes. For reference, the black curve shows the same solar metallicity continuous models plotted in the upper panels. The cyan points show the location of “pure” starburst models. The pure starbursts begin forming their stars between 5×10^8 years and 10^6 years ago and form stars at a constant rate. The yellow and green points show the location of continuous models with superposed pure starbursts of differing amplitude. The yellow points are for strong bursts that contribute between 0.1 and 50% of the total mass in stars. The green points are for weak bursts that contribute between 0.005 and 0.1% of the total stellar mass. Superposing an ongoing starburst onto an underlying continuous model moves galaxies to lower values of

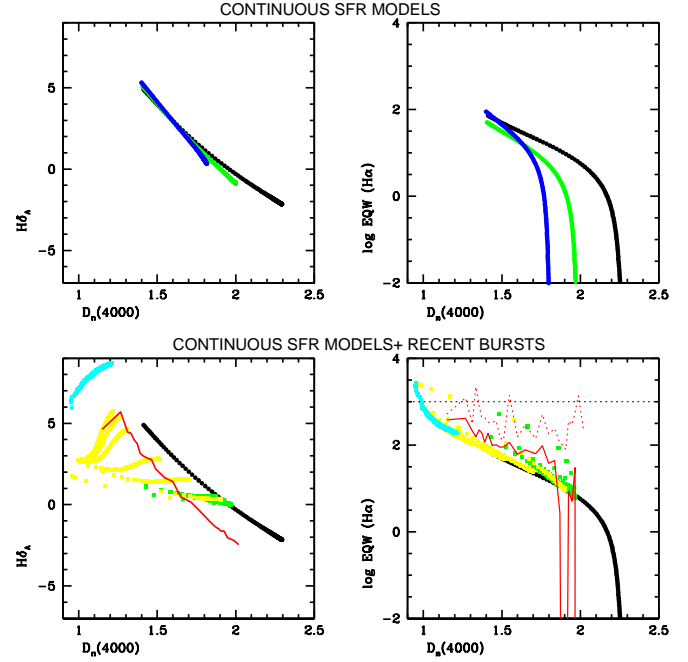


Figure 10. Top panels: Loci occupied by galaxies in the $H\delta_A$ versus $D_n(4000)$ (left) and EQW H α versus $D_n(4000)$ planes that have had continuous star formation histories. Black, green and blue curves show results for solar, 0.5 solar and 0.25 solar metallicity models. Bottom panels: Model with recent bursts superposed upon the grid of models with continuous star formation histories and solar metallicity (black curve). The yellow points are for strong bursts that contribute between 0.1 and 50% of the total mass in stars. The green points are for weak bursts that contribute between 0.005 and 0.1% of the mass. The cyan points show the location of “pure” starburst model with no underlying older stellar population. The solid and dotted red curves show the median and 90th percentile relations shown in the two left-hand panels of Figure 3 for the inner stellar populations of low mass galaxies with $10 < \log M_* < 10.5$.

$D_n(4000)$. Interestingly, the starburst moves the galaxy below the continuous model locus in the $H\delta_A$ versus $D_n(4000)$ plane, but moves the galaxy *along this locus* in the EQW H α versus $D_n(4000)$ plane. The small smattering of points that are displaced well above the locus are for extremely young bursts that are less than a few million years old superposed on relatively old stellar populations.

Note that even with very young bursts, it is not possible to reach H α equivalent width values close to a thousand at intermediate values of $D_n(4000)$, as observed in the central regions of some of the outlier galaxies. For reference, we have plotted the median and 90th percentile relations shown in the two left-hand panels of Figure 3 for the inner stellar populations of low mass galaxies with $10 < \log M_* < 10.5$ as red solid and dotted lines. As can be seen, the 90th percentile in the distribution of EQW (H α) at fixed $D_n(4000)$ is not reachable even for extremely young bursts, particularly at the larger $D_n(4000)$ values.

I now turn to a very simple first exploration of the effect of changing the upper mass end of the IMF. In the Galactic Center, the upper-end of the IMF slope has been con-

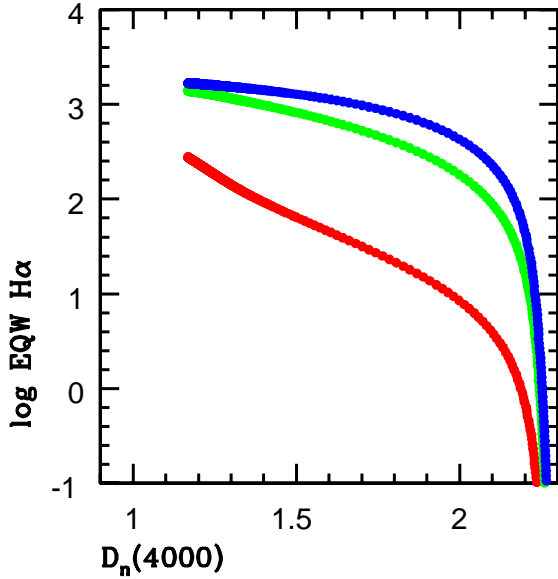


Figure 11. Loci occupied by galaxies in the EQW $H\alpha$ versus $D_n(4000)$ plane that have had continuous star formation histories. The red curve shows results for the fiducial IMF, the green and blue curves show results for the two IMF changes described in the text (green is for case (i) and blue for case (ii)).

strained using the K-band luminosity function of luminous early-type stars located in two disk-like structures in the inner 0.5 pc of the Galactic bulge. Paumard et al (2006) obtain a best fit mass function with a considerably flatter slope than the standard Salpeter one ($dN/dm = m^{-0.85}$ compared to $dN/dm = m^{-2.35}$). Because of the very young inferred ages of the stars, it was concluded that most of the stars must have formed in place from gas in the observed disks, rather than having migrated inwards from birth clouds at larger radius. In more recent work, Lu et al (2013) estimate a slope $dN/dm = m^{-\alpha}$, with $\alpha = 1.5 - 1.9$ for young stars with masses above $10 M_{\odot}$, considerably flatter than Salpeter but not as extreme as that estimated in earlier work.

Motivated by these results, Figure 11 explores the effect of flattening the IMF slope away from the Salpeter value above some characteristic stellar mass. The purpose here is to examine the outer boundaries of the possible variations in $H\alpha$ equivalent width under the most extreme IMF changes. Results from two models are compared with the fiducial case of solar metallicity continuous star formation models with Salpeter IMF (red curves) :

- (i) a model where $\alpha = 0.5$ above $7 M_{\odot}$ (blue curves)
- (ii) a model where $\alpha = 0.8$ above $10 M_{\odot}$ (green curves)

As can be seen, these models result in $H\alpha$ equivalent widths that are a factor 4-7 higher at a fixed value of $D_n(4000)$. Wolf Rayet emission features are predicted by the Starburst99 code, but it is difficult to combine these with the stellar continuum predictions in a robust way, so we will defer detailed examination of red and blue bump predictions to future work.

Another issue that should be addressed in future work

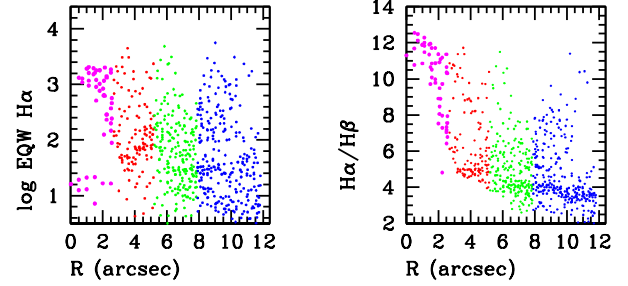


Figure 12. The $H\alpha$ equivalent width and Balmer decrement profiles for the recent major merger remnant pictured in the bottom row, third column of the outlier galaxy image montage shown in Figure 8.

is the dust correction. Almost all the galaxies in the outlier sample have Balmer decrement profiles that rise towards the central region of the galaxy. This means that the corrections that have to be made in order to estimate the true production rate of ionizing photons become progressively larger at smaller radii, which will complicate quantitative interpretation of the results. One might also ask whether some fraction of the massive star population could simply be so deeply embedded in dust so as to be completely invisible at optical wavelengths.

One important diagnostic of the clumpy nature of the dust in the central regions of the outlier galaxies in our sample, is the scatter in the Balmer decrement values measured for different spaxel spectra at the same radius. The scatter in $H\alpha/H\beta$ at fixed R/R_{50} is small in all the examples shown in Figures 8 and 9. Only one galaxy in our sample is substantially different – this is the recent major merger remnant pictured in the bottom row, third column of the outlier galaxy image montage shown in Figure 8. The $H\alpha$ equivalent width and Balmer decrement profiles for this galaxy are shown in Figure 12. The scatter in both is very much larger in this galaxy. The Balmer decrement values appear to lie along two tracks, a high and a low attenuation one, perhaps indicating incomplete mixing of the interstellar medium components of the two progenitor galaxies that merged to form this object.

Even if the dust distribution in the centers of most of the outlier galaxies is homogeneous, in order to compare the observational measurements with population synthesis model predictions, both the Balmer line emission and the stellar continuum fluxes have to be properly dust-corrected. Figure 13 shows how such corrections vary systematically between the outliers and the control sample. The ratio $EQW(H\alpha)/EQW(H\beta)$, which includes the measured stellar continuum at the wavelengths of the two Balmer lines, is plotted as a function of the standard Balmer decrements $H\alpha/H\beta$ for spaxels with $R/R_{50} < 0.5$ for control galaxies (black) and for outliers (red). The two samples largely overlap each other for Balmer decrement values up to ~ 6 . The outlier sample shows a tail of Balmer decrement values extending out to values in excess of 8, where the ratio $EQW(H\alpha)/EQW(H\beta)$ appears to saturate at a fixed value. These high dust attenuation spaxels originate from the very central regions of the outliers. Once again, more detailed modelling via full spectrum-fitting techniques (e.g. Wilkin-

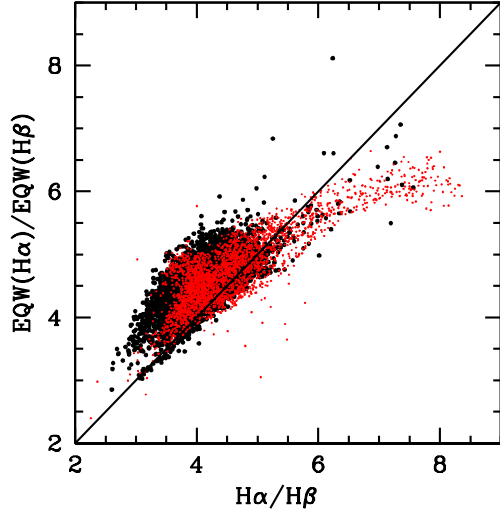


Figure 13. The ratio $\text{EQW}(\text{H}\alpha)/\text{EQW}(\text{H}\beta)$, which includes the measured stellar continuum at the wavelengths of the two Balmer lines, is plotted as a function of the standard Balmer decrements $\text{H}\alpha/\text{H}\beta$ for spaxels with $R/R_{50} < 0.5$ for control galaxies (black) and for outliers (red).

son et al 2017) is required for more detailed interpretation and will be the subject of future work.

6.2 Growth of black holes and the AGN connection

Dense inner galactic bulges with an excess population of young massive Wolf Rayet stars are likely to be very interesting sites for studying black hole growth and accretion processes. The most massive of these stars will form stellar black holes at the end of their evolution and will also expel substantial material in winds that may later cool and accrete onto the central black hole if it is present. Large populations of stellar mass black holes may also merge in dense environments to form a new black holes. Within the context of the IFU survey at hand, further progress in this area could be made by searching for and studying *transition objects*, i.e. galaxies with extreme central starbursts that will later become AGN.

Recall that the outlier sample is selected in the plane of $\text{EQW H}\alpha$ versus $D_n(4000)$ and is restricted to galaxies with central values of $D_n(4000)$ less than 1.6, i.e. to bulges with young to middle-aged stellar populations. There is one galaxy among the sample of 15 that has significantly higher ionization parameter than the other outlier galaxies and may plausibly be considered as an example of a transition object. This is the interacting spiral shown in the top row, 3rd column of Figure 7; its traditional name is IC 0910, classified as a LINER in the catalogue of Veron-Cetty & Veron (1996).

Figure 14 shows a compilation of radial profiles for this object. Note that this galaxy is among those with the strongest Wolf Rayet signatures. It is unusual in that it shows strong blue bump and red bump excesses, signifi-

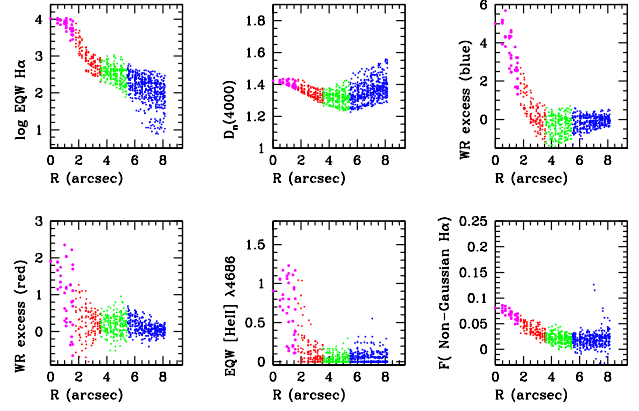


Figure 14. Radial profiles for a variety of stellar and ionized gas diagnostics. Magenta, red, green and blue points show spaxel located within $0-0.3 R_{50}$, $0-0.3 R_{50}$, $0-0.3 R_{50}$, and $0-0.3 R_{50}$, respectively. These results are for the outlier galaxy in the top row, third column in the first montage in Figure 7.

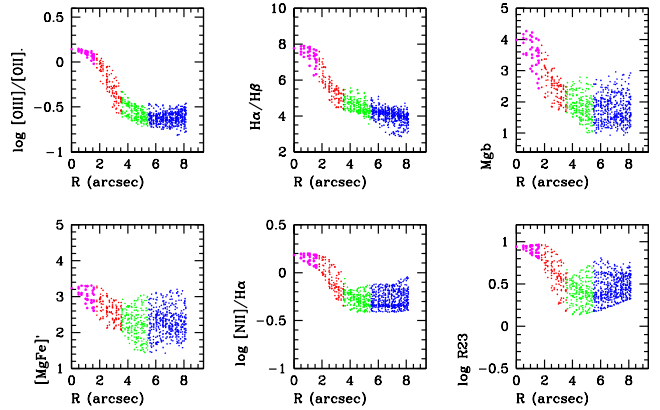


Figure 14 – continued More radial profiles.

cant central $[\text{HeII}]\lambda 4686$ emission and clear non-Gaussian $\text{H}\alpha$ profiles in the centre of the galaxy. Most of the outliers only exhibit a subset of these signatures. It is also the outlier where the profiles of stellar and ionized gas metallicity and dust rise most strongly near the centre of the galaxy and the central BPT line ratios are consistent with AGN rather stellar ionization.

One question is whether the observed non-Gaussian signature in the $\text{H}\alpha$ emission line is indicative of the presence of an outflow. Another question concerns the extent to which the outflow is influencing the gas in the galaxy. A first attempt to answer this question is made in Figure 15 where the ratio of the velocity dispersion of the $\text{H}\alpha$ emitting gas to the stellar velocity dispersion is plotted as a function of $\log \text{EQW H}\alpha$ for individual spaxel spectra. The black points show measurements from spaxels located within $0.3 R_{50}$ for the control galaxies and red points are for the outlier galaxies. Spaxels from the galaxy highlighted in this section are coloured as magenta points. From this, it can be seen that the galaxy selected as a possible transition object is unique. The ratio $\sigma(\text{gas})/\sigma(\text{stars})$ lies between 0.1 and 1 for almost all the measurements in the central regions of both the outlier and the control sample. For the transition ob-

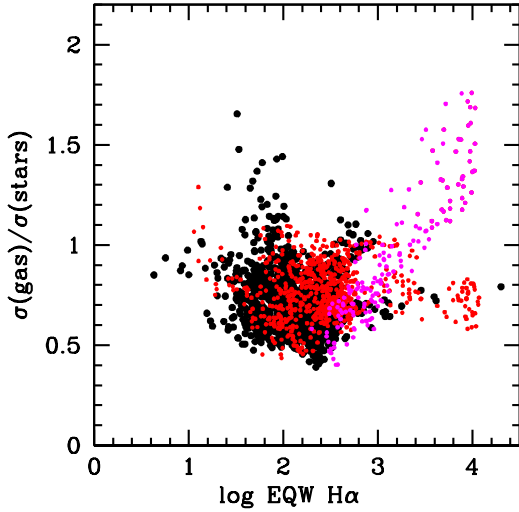


Figure 15. The ratio of the velocity dispersion of the H α emitting gas to the stellar velocity dispersion is plotted as a function of log EQW H α for individual spaxel spectra. The black points show measurements from spaxels located within $0.3 R_{50}$ for the control galaxies and red points are for the outlier galaxies. Spaxels form the galaxy highlighted in this section are coloured as magenta points.

ject, $\sigma(\text{gas})/\sigma(\text{stars})$ rises to values of 1.5–1.7 at the very center of the galaxy. This indicates that feedback from a centrally accreting black hole or from winds generated by massive stars is stirring up the gas very significantly in this particular system. It would obviously be very useful to increase sample sizes in future work and study whether it is possible to map out a clear evolutionary sequence in central stellar population properties, as well as in gas and stellar kinematics. In recent work, D’Agostino et al (2019) suggest that resolved observations of the velocity dispersion of gas in AGN can be used as a diagnostic of where shock-heating processes are important.

6.2.1 A more detailed examination of Wolf Rayet features

W-R galaxies are usually defined as those galaxies in whose integrated spectra a broad emission feature at He II $\lambda 4686$ attributable to Wolf-Rayet stars has been detected (Conti, 1991). W-R galaxies identified this way have been found to span the full range of stellar masses and morphologies as the ordinary galaxy population, but are exclusively found in galaxies with the bluest colors and highest star formation rates for their mass (Brinchman et al 2008; Liang et al 2020). A blue bump selection method has been demonstrated to produce samples where detection of the red bump is relatively rare (Schaerer & Vacca 1998; Brinchmann et al 2008).

It is thus intriguing that the frequency with which the red bump is detected in the outlier sample is considerably higher than for the blue bump. A detailed physical interpretation of this finding lies beyond the scope of this paper.

One question is whether the red bump can be clearly

resolved into individual emission lines, which might assist in further interpretation of this feature. Wolf-Rayet stars are divided into 3 classes based on their spectra, the WN stars (nitrogen dominant, some carbon), WC stars (carbon dominant, no nitrogen), and the rare WO stars with $C/O < 1$. The broad C IV $\lambda 5808$ emission line dominates the red bump and its strength relative to the blue bump should be indicative of the WC-to-WN star ratio. Wolf-Rayet star features could, in principle, be very IMF sensitive. More detailed research is required, however, to properly constrain the progenitor masses of different Wolf-Rayet classes. Whether or not the WC-to-WN star ratio can be regarded as a constraint on the IMF or a diagnostic of the formation rate of stellar mass black holes remains a topic of controversy (Sander et al 2019).

Figure 16 presents a series of 4 spaxel spectra over the wavelength range spanning the red bump Wolf Rayet feature for the galaxy discussed in the previous subsection. The spectra are arranged in order of increasing distance from the centre of the galaxy. The positions of the the main emission line features are indicated in each panel. The C IV $\lambda 5808$ line is clearly detectable in the first two of the central spaxel spectra and shows a broad component. The Wolf Rayet features are particularly strong in this galaxy; spectral stacking may be a way to conduct systematic studies of Wolf-Rayet signatures for larger samples of bulges in future work in order to study possible variations in the upper IMF more systematically.

7 SUMMARY

The goal of this paper has been to search for galaxy centers with clear indications of unusual stellar populations. The motivation for this is the finding that the stellar content of our own Galactic Center is surprisingly exotic. Two inner disks of massive young stars are found that must have formed very recently with an initial mass function that is flatter than Salpeter at high stellar masses. These unusual stellar populations are only found within the central parsec of our own Galaxy and would be undetectable in external galaxies with current telescopes and instrumentation. The hypothesis that is tested in this analysis is that there are populations of bulges where similar phenomena extend over much larger scales, where the total mass in young high mass stars is much larger, and where the impact of these stars on the galaxy as they evolve could be quite dramatic.

Out of a sample of 668 face-on galaxies with stellar masses in the range $10^{10} - 10^{11} M_{\odot}$, I identify 15 galaxies with young to intermediate age inner stellar populations and where stellar population gradients show unusual patterns in their central regions. In these galaxies, the 4000 Å break is either flat or rising towards the center of the galaxy, indicating that the central regions host evolved stars, but the H α equivalent width also rises in the central regions, indicating the presence of increasing amounts of strongly ionized gas. The ionization parameter [OIII]/[OII] is typically low in these galactic centers, indicating that ionizing sources are stellar rather than AGN. Wolf Rayet features characteristic of hot young stars are often found in the spectra and these also get progressively stronger at smaller galactocentric radii.

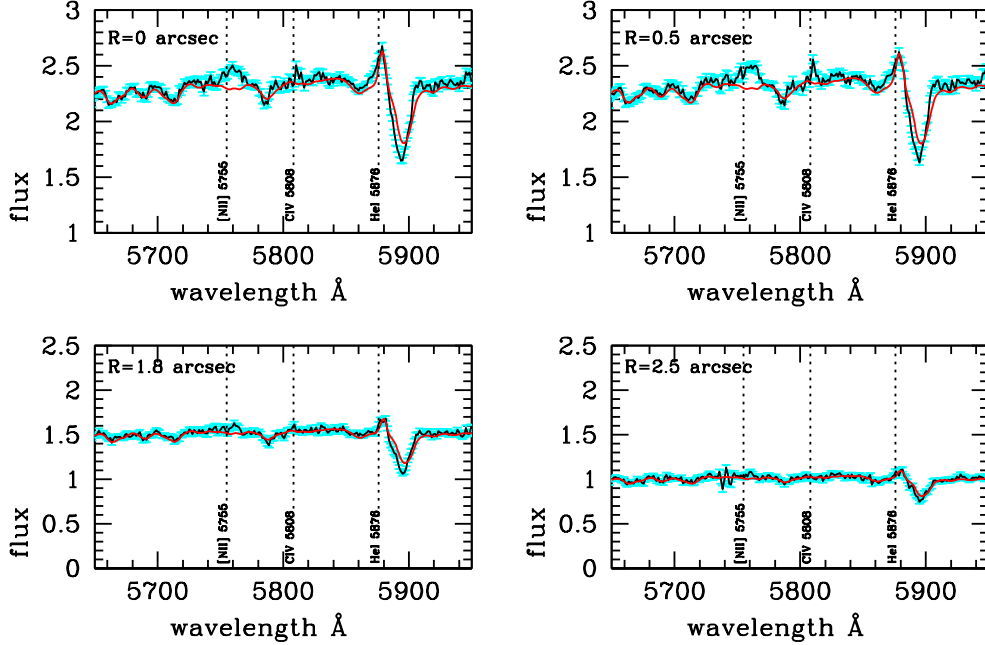


Figure 16. A series of 4 spaxel spectra over the wavelength range spanning the red bump Wolf Rayet feature for the same galaxy as in the previous figure. The spectra are arranged in order of increasing distance from the centre of the galaxy. The positions of the the main emission line features are indicated in each panel. The C IV $\lambda 5808$ line is clearly detectable in the first two central spaxel spectra and shows a broad component.

These outliers are compared to a control sample of galaxies of similar mass with young inner stellar populations, but where the gradients in $H\alpha$ equivalent width and 4000 \AA break follow each other more closely. It is demonstrated that central Wolf Rayet excesses are much more common in the outliers, that the outliers have higher central stellar and ionized gas metallicities, and that they are also much more frequently detected in the radio compared to the control galaxies. I highlight one outlier where the ionized gas is clearly being strongly perturbed and blown out either by massive stars after they explode as supernovae, or by energy injection from matter falling onto black holes.

Detailed quantitative comparisons with and inferences from stellar population synthesis models will be the subject of future work. I have highlighted a number of the stumbling blocks with regard to accurate population synthesis modelling that will first need to be overcome. It will also be interesting to probe the structure and kinematics of the gas and stellar distributions at the centers of the closest of these outliers with high resolution spatially resolved observations, particularly at radio and sub-millimetre wavelengths. It would also be very interesting to understand the connection between the outlier population studied in this paper and the nuclear star cluster phenomenon. Do the objects selected using our methodology constitute the formation phase of the most massive of such systems? The qualitative similarities with the stellar properties of the nuclear star cluster in our own Milky Way hints that there is much left to be understood about the role of very massive stars in the formation and evolution of all galactic bulges.

Acknowledgements

I thank Reinhard Genzel, Eckhardt Sturm, Thorsten Naab and Claudia Maraston for helpful discussions about this work.

Funding for SDSS-IV has been provided by the Alfred P. Sloan Foundation and Participating Institutions. Additional funding towards SDSS-IV has been provided by the US Department of Energy Office of Science. SDSS-IV acknowledges support and resources from the Centre for High-Performance Computing at the University of Utah. The SDSS web site is www.sdss.org. SDSS-IV is managed by the Astrophysical Research Consortium for the Participating Institutions of the SDSS Collaboration including the Brazilian Participation Group, the Carnegie Institution for Science, Carnegie Mellon University, the Chilean Participation Group, the French Participation Group, Harvard-Smithsonian Center for Astrophysics, Instituto de Astrofísica de Canarias, The Johns Hopkins University, Kavli Institute for the Physics and Mathematics of the Universe (IPMU)/University of Tokyo, Lawrence Berkeley National Laboratory, Leibniz Institut für Astrophysik Potsdam (AIP), Max-Planck-Institut für Astronomie (MPIA Heidelberg), Max-Planck-Institut für Astrophysik (MPA Garching), Max-Planck-Institut für Extraterrestrische Physik (MPE), National Astronomical Observatory of China, New Mexico State University, New York University, University of Notre Dame, Observatorio Nacional/MCTI, the Ohio State University, Pennsylvania State University, Shanghai Astronomical Observatory, United Kingdom Participation Group, Universidad Nacional Autónoma de México, University of

Arizona, University of Colorado Boulder, University of Oxford, University of Portsmouth, University of Utah, University of Virginia, University of Washington, University of Wisconsin, Vanderbilt University and Yale University.

Data availability: The data is available upon reasonable request to the corresponding author.

REFERENCES

- Balcells M., Peletier R. F., 1994, *AJ*, 107, 135
- Baldwin J. A., Phillips M. M., Terlevich R., 1981, *PASP*, 93, 5
- Balogh M. L., Morris S. L., Yee H. K. C., Carlberg R. G., Ellingson E., 1999, *ApJ*, 527, 54
- Becklin E. E., Neugebauer G., 1968, *ApJ*, 151, 145
- Belfiore F., et al., 2016, *MNRAS*, 461, 3111
- Belfiore F., et al., 2019, *AJ*, 158, 160
- Blanton M. R., et al., 2017, *AJ*, 154, 28
- Brinchmann J., Kunth D., Durret F., 2008, *A&A*, 485, 657
- Bruzual G., Charlot S., 2003, *MNRAS*, 344, 1000
- Bundy K., et al., 2015, *ApJ*, 798, 7
- Calzetti D., 2001, *PASP*, 113, 1449. doi:10.1086/324269
- Cappellari M., Emsellem E., 2004, *PASP*, 116, 138
- Conti P. S., 1991, *ApJ*, 377, 115
- Conroy C., Gunn J. E., White M., 2009, *ApJ*, 699, 486
- D’Agostino J. J., Kewley L. J., Groves B. A., Medling A., Dopita M. A., Thomas A. D., 2019, *MNRAS*, 485, L38. doi:10.1093/mnras/slz028
- de Jong R. S., 1996, *A&AS*, 118, 557
- Drory N., et al., 2015, *AJ*, 149, 77
- Eldridge J. J., Stanway E. R., 2009, *MNRAS*, 400, 1019
- Ferrarese L., Merritt D., 2000, *ApJL*, 539, L9. doi:10.1086/312838
- Förster Schreiber N. M., et al., 2018, *ApJS*, 238, 21
- Gebhardt K., Bender R., Bower G., Dressler A., Faber S. M., Filippenko A. V., Green R., et al., 2000, *ApJL*, 539, L13. doi:10.1086/312840
- Genzel R., 1996, *LNP*, 474, 175, *LNP...474*
- Genzel R., et al., 2003, *ApJ*, 594, 812
- Gunn J. E., et al., 2006, *AJ*, 131, 2332
- Heckman T. M., Kauffmann G., Brinchmann J., Charlot S., Tremonti C., White S. D. M., 2004, *ApJ*, 613, 109
- Hickox R. C., et al., 2009, *ApJ*, 696, 891
- Kauffmann G., et al., 2003, *MNRAS*, 346, 1055
- Kewley L. J., Groves B., Kauffmann G., Heckman T., 2006, *MNRAS*, 372, 961
- Kroupa P., 2001, *MNRAS*, 322, 231
- Law D. R., et al., 2015, *AJ*, 150, 19
- Law D. R., et al., 2016, *AJ*, 152, 83
- Leitherer C., et al., 1999, *ApJS*, 123, 3
- Leitherer C., Ekström S., Meynet G., Schaerer D., Agienko K. B., Levesque E. M., 2014, *ApJS*, 212, 14
- Levin Y., Beloborodov A. M., 2003, *ApJL*, 590, L33
- Liang F.-H., et al., 2020, *ApJ*, 896, 121
- MacArthur L. A., González J. J., Courteau S., 2009, *MNRAS*, 395, 28
- Martins, L.P., González Delgado, R.M., Leitherer, C., Cerviño, M., and Hauschildt, P.: 2005, *Monthly Notices of the Royal Astronomical Society* **358**, 49.
- Martins, L.P., González Delgado, R.M., Leitherer, C., Cerviño, M., and Hauschildt, P.: 2005, *Monthly Notices of the Royal Astronomical Society* **358**, 49.
- McGaugh S. S., Schombert J. M., 2014, *AJ*, 148, 77. doi:10.1088/0004-6256/148/5/77
- Neumayer N., Seth A., Boeker T., 2020, arXiv, arXiv:2001.03626
- Paumard T., et al., 2006, *ApJ*, 643, 1011
- Portegies Zwart S. F., McMillan S. L. W., 2002, *ApJ*, 576, 899
- Rees M. J., 1978, *PhyS*, 17, 193
- Sander A. A. C., Hamann W.-R., Todt H., Hainich R., Shenar T., Ramachandran V., Oskinova L. M., 2019, *A&A*, 621, A92. doi:10.1051/0004-6361/201833712
- Schaerer D., Vacca W. D., 1998, *ApJ*, 497, 618
- Schödel R., Feldmeier A., Neumayer N., Meyer L., Yelda S., 2014, *CQGra*, 31, 244007
- Smee S. A., et al., 2013, *AJ*, 146, 32
- Smith N., 2014, *ARA&A*, 52, 487. doi:10.1146/annurev-astro-081913-040025
- Terndrup D. M., Davies R. L., Frogel J. A., Depoy D. L., Wells L. A., 1994, *ApJ*, 432, 518
- Thomas D., Maraston C., Bender R., Mendes de Oliveira C., 2005, *ApJ*, 621, 673
- Vazdekis A., Koleva M., Ricciardelli E., Röck B., Falcón-Barroso J., 2016, *MNRAS*, 463, 3409
- Veron-Cetty M.-P., Veron P., 1996, *A&AS*, 115, 97
- Wake D. A., et al., 2017, *AJ*, 154, 86
- Westfall K. B., et al., 2019, *AJ*, 158, 231
- Wilkinson D. M., Maraston C., Goddard D., Thomas D., Parikh T., 2017, *MNRAS*, 472, 4297
- Worthey G., Ottaviani D. L., 1997, *ApJS*, 111, 377
- Yan R., et al., 2016, *AJ*, 152, 197